Seismic effects of the Caloris basin impact, Mercury

by

Jiangning Lü

Bachelor of Science, Peking University, 2002
Master of Science, Geophysics, Peking University, 2005

Submitted to the Department of Earth, Atmospheric and Planetary Sciences
In partial fulfillment of the requirements for the degree of
Master of Science in Earth, and Planetary Sciences
At the
MASSACHUSETTS INSTITUTE OF TECHNOLOGY
September 2011

ARCHIVES
MASSACHUSETTS INSTITUTE OF TECHNOLOGY
NOV 2 2 2011
LIBRARIES

© Massachusetts Institute of Technology 2011. All rights reserved.

Author ....
Department of Earth, Atmospheric and Planetary Sciences
August 15, 2011

Certified by ....
Maria T. Zuber
E.A. Griswold Professor of Geophysics and Planetary Science
Thesis Supervisor

Accepted by ....
Daniel Rothman
Professor of Geophyiscs
Chair, EAPS Graduate Committee

Seismic effects of the Caloris basin impact, Mercury

by

Jiangning Lü

Submitted to the Department of Earth, Atomospheric and Planetary Sciences
On August 15, 2011, in partial fulfillment of the
Requirements for the degree of
Master of Science in Earth, and Planetary Sciences

Abstract

Striking geological features on Mercury's surface have been linked to tectonic disruption associated with the Caloris impact and have the potential to provide information on the interior structure of Mercury. The unusual disrupted terrain located directly at the antipode of the 1500-km-diameter Caloris basin could have plausibly formed as a consequence of focused seismic waves generated by the massive impact event. In this paper, we revisit the antipodal seismic focusing effects of the Caloris impact by developing physically consistent structure models for Mercury and parameterized seismic source models for the Caloris impact. If the focused seismic body waves caused the disrupted terrain, then the amplitudes of the waves and the areal extent of surface disruptions could be used for estimating the seismic energy imparted by the impact.

In this study, we show that effects of direct body waves are small relative to those of the focused guided waves. Two types of guided waves are generated by the Caloris impact. One is the conventional Rayleigh wave generated by the impact. The second is the mantle guided waves trapped between the core and the free surface. Mantle guided waves, not mentioned in previous studies, may have played an important role in the creation of the disrupted terrain. We find that the early core state has only moderate effects on the antipodal response to the Caloris impact. The fact that the zone of predicted disruption for both fluid and solid core cases is smaller than the observed region of chaotic terrain suggests either that the antipodal response to the Caloris impact may have been modulated by the shallow structure of Mercury, or that the energy imparted by the impact was larger than those used in this study.

Thesis Supervisor: Maria T. Zuber
Title: E.A. Griswold Professor of Geophysics

Acknowledgements

First and foremost I would like to express my deep and sincere gratitude to my supervisor Professor Maria Zuber, Head of the Department of Earth, Atmospheric and Planetary Sciences, MIT. She has been very helpful and supportive academically and emotionally through the rough road. It is also a great honor for me to have the opportunity to work with Professor Nafi Toksöz. He has been a friend, guide and philosopher. I'm also indebted to Professor Bradford Hager for admitting me to EAPS and giving me this life-changing opportunity. I thank Dr. Youshun Sun for making available his support in a number of ways. I also thank Dr. Yingcai Zheng for his important contribution to this project. Lastly, I offer my regards and blessings to all of those who supported me in any respect during this time period at MIT.

Contents

1 Introduction 10

2 Physical process and model 13

2.1 Basin-forming impact 13

2.2 Seismic wave propagation through Mercury 16

2.2.1 1-D seismic structure of Mercury 17

2.2.2 Seismic wave attenuation 19

2.2.3 Body and surface waves in Mercury 20

2.2.4 Various source effects 24

2.3 The Caloris impact and antipodal disruption 27

3 Results and discussion 32

3.1 Role of internal state 32

3.2 Role of antipodal seismic focusing 33

3.3 Comparison with previous studies 34

4 Summary and conclusions 38

Bibliography 41

List of Figures

Figure 1. The Caloris basin (blue circle) is estimated at about 1550 km in diameter based on MESSENGER's images. The basin is larger than the estimate from the 1974 Mariner 10's images (about 1300 km, yellow circle). The visible seam is caused by mosaicking of images collected in different lighting conditions. Credit: NASA/Johns Hopkins University Applied Physics Laboratory/Carnegie Institution of Washington. (http://messenger.jhuapl.edu) 11

Figure 2. Images of the hilly and lineated terrain at the antipode of the Caloris basin from Mariner 10 and MESSENGER. The location of the antipode to the center of the Caloris basin is marked by red stars (Solomon et al., 2001; Murchie et al., 2008). The large, smooth-floored crater just left of center is 150 kilometers in diameter. Credit: NASA/Johns Hopkins University Applied Physics Laboratory/Carnegie Institution of Washington. (http://messenger.jhuapl.edu) 14

Figure 3. Top: Approximation to the function sin(x)/x used in modeling the source spectrum. Bottom: a common approximation uses a single corner frequency f_c. The flat segment extending to zero frequency gives M_0. (Stein and Wysession, 2003). 16

Figure 4. Two end-member physically consistent 1-D seismic structure models of Mercury. The blue curves show the property profiles for a model with a molten core; the red curves are for a model with a solid core. The thin black curves are profiles of PREM scaled to Mercury. In c), the solid curves show P wave velocities, and the dashed or dot-dashed curves show S wave velocities. 18

Figure 5. Possible range of attenuation of seismic waves in Mercury. Parameters Q_α

(dashed lines) and Q_β (solid lines) control the attenuation of *P* and *S* waves, respectively. Blue, model with molten core; red, model with solid core. Right: lower-bound model with least attenuation (higher Q values), which is similar to Earth. Center: one optimized model. Left: upper-bound model with most attenuation (lower Q values). 20

Figure 6. Seismic ray paths for the direct *P* wave, which travels in the mantle, and for the core phase *PKP*. The source is at the surface. 22

Figure 7. Vertical (a) and radial (b) displacements computed using the DSM at different angular distances from the source. The seismic source is a moment magnitude M_W 6 event. The corner frequency $f_c = 0.1$ Hz, the source spectrum follows ω^1-type scaling, and the depth of burial $H = 100$ km. The high end of the frequency bandwidth in the computation is 1 Hz and the final seismograms are bandpass filtered between 0.001 Hz and 0.5 Hz. The red lines are *P* and *PKP* wave travel-time curves predicted by ray tracing. 23

Figure 8. Vertical displacements (normalized by source area) at the antipodal point (i.e., epicentral distance 180 degrees) for different area sources. We assume the area source is circular and the force direction is vertical. The source depth is at 10 km. The computational bandwidth is between 0 and 0.5 Hz and the final result is filtered between 0.001 Hz and 0.1 Hz. 24

Figure 9. The effect of different scaling laws, ω^1- and ω^2-type, for the source amplitude spectrum and different cutoff frequencies (f_c) on the antipodal seismogram produced by a point explosion at 100 km depth. We did not plot the case f_c=100 mHz because the waveform is same as f_c=50 mHz. The computational bandwidth is between 0 and 1 Hz. 26

Figure 10. Antipodal seismograms for different source depths, *H.* The amplitudes are relative. In this example, the double-couple time history is a delta function and the resultant displacement is bandpass filtered between 0.001 Hz and 0.1 Hz. The source is a point explosion and the cutoff frequency f_c is 0.1 Hz of the ω^1 type. 27

Figure 11. Displacement histories determined by normal mode summation at different angular distances from the source. The angular distances are marked at the right side of the seismograms (from 5 to 178°). The seismic source parameters used for this model include: scalar moment $M_0 = 0.86 \quad 10^{34}$ dyne-cm, corner frequency f_c = 100 mHz, depth of burial H = 100 km. 28

Figure 12. Displacements and principal stresses at an angular distance of 5° (215 km) from the antipode. The source parameters and internal state model are the same as Fig. 6. The peak amplitude of displacement is about 150 m; the peak amplitude of stress is about 250 MPa. 30

Figure 13. Range of static moment M_0 for different models that produce the same surface disruption. Surface waves dominate for the group of models in red; body waves dominate for models in blue. Models marked as circles have a solid core; models marked as squares have a molten core. 34

Figure 14. Variation of peak stress with angular distance from the antipode, located at the right side of each plot (180° of angular distance from the source). Each model is normalized by the value at the angular distance of 135°. The two groups of models shown here have different depths of the equivalent explosion source. (a) 20 km deep source, for which surface waves dominate. (b) 100 km deep source, for which body waves dominate.

Blue and red curves are models with molten and solid cores, respectively. 35

Chapter 1

Introduction

Mercury, an end-member terrestrial planet with a high bulk density (Anderson et al., 1987), holds a crucial position in understanding the formation and evolution of the terrestrial planets. Among the interesting features of this body are its presumed large, iron-rich core and its present-day dipole magnetic field (Connerney and Ness, 1988; Purucker et al., 2009), which appears to be a consequence of dynamo action. While historically all models of the interior structure (Siegfried and Solomon, 1974; Harder and Schubert, 2001) have large metallic cores, there has been considerable debate about the evolution of the planet's internal state, particularly the core state. The giant Caloris impact, which probably occurred during early solar system history (~4 Ga), has left striking features on Mercury's surface. The 1500-km-diameter Caloris basin is arguably the most prominent physiographic feature on the surface (Fig. 1); discovered during Mariner 10 flybys (Murray et al., 1974), the basin was fully revealed (Murchie et al., 2008) by the MErcury Surface, Space ENvironment, GEochemistry, and Ranging (MESSENGER) mission (Solomon et al., 2007). An anomalous region of hilly and lineated terrain (Melosh and McKinnon, 1988) with an area of at least 500,000 km^2, is located directly at the antipode of the Caloris basin (Murray et al., 1974) (Fig. 2). This unusual disrupted terrain consists of 5-10 km wide hills and depressions with heights of 0.1-1.8 km that disrupt pre-existing landforms (Murray et al., 1974). Schultz and Gault (1975) first suggested that the antipodal formation was produced by impact-induced seismic waves, which propagated through the planet and were greatly magnified at the antipodal region because of seismic focusing. Early simulations showed that the Caloris event could have produced vertical ground movement of about 1 km at the antipode (Hughes et al., 1977). If the focused seismic waves did cause the antipodal disrupted terrain, then the amplitudes of the seismic waves and the areal extent of surface disruption would have been influenced by the energy of the impact and, for body waves, Mercury's core size and its physical state, and, for surface waves, crustal and upper mantle properties. Since the earlier studies, there have been significant improvements in computing capability as well as in understanding of the physical properties of materials likely to compose Mercury's interior. We are motivated to explore the impact-induced seismic wave propagation and antipodal focusing seismic effects of Caloris impact using modern methods of seismic analysis appropriate to the level of constraints on the problem. We begin by developing one-dimensional (1-D), physically consistent models for the internal structure of Mercury as well as parameterized seismic source models for the Caloris impact. We then examine the effects of various parameters on the amplitudes of the seismic waves that reach the antipodal region.

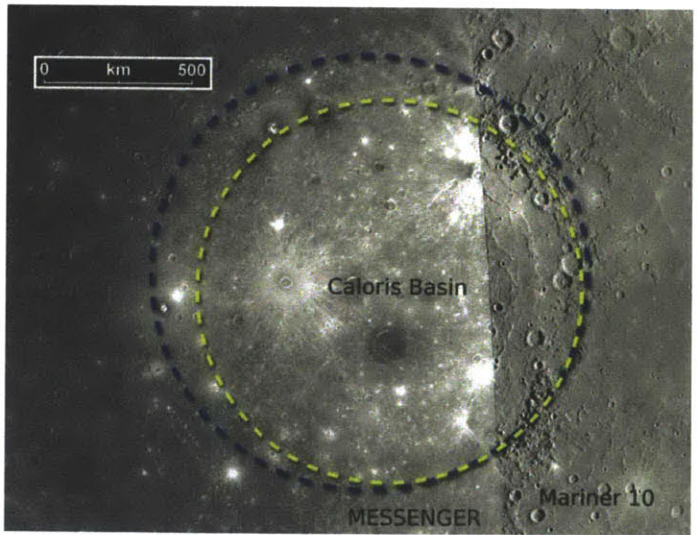

Fig. 1. The Caloris basin (blue circle) is estimated at about 1550 km in diameter based on MESSENGER's images. The basin is larger than the estimate from the 1974 Mariner 10's images (about 1300 km, yellow circle). The visible seam is caused by mosaicking of images collected in different lighting conditions. Credit: NASA/Johns Hopkins University Applied Physics Laboratory/Carnegie Institution of Washington. (http://messenger.jhuapl.edu)

Chapter 2

Physical process and model

Modeling the impact and its physical consequences requires consideration of a wide range of spatial and temporal scales, as well as markedly different physical processes. For tractability we may deconstruct the event and its aftermath into three component parts: 1) the basin-forming impact process, 2) wave propagation through the planet, and 3) disruption at the antipode. First, the basin-forming impact generates shock waves and involves a sudden increase in pressure, which causes nonlinear deformation that can melt and even vaporize rock. This shock wave of pressure decreases rapidly as it expands, and it will decay eventually to linearly elastic seismic waves. Second, the elastic seismic wave is a nearly spherical *P* wave initially, and generates SV and Rayleigh waves when it impinges upon the surface and interfaces within Mercury. These waves propagate through the planet and the magnitudes are amplified at the antipode to the impact. Finally, the dynamic stresses due to seismic waves are superimposed on the pre-existing static stresses. Wave propagation involves both compression and rarefaction and therefore both tensile and compressive stresses are generated. When the tensile stress exceeds the tensile strength of Mercury's crust, disruption will occur. In the following part of this section, we parameterize the complex multiple physical processes into simple models with assumptions and approximations.

2.1. Basin-forming impact

Due to similarities of impacts to explosive sources (Melosh, 1989), we model the hypervelocity Caloris impact as an explosion source near the surface of Mercury. Both impacts and explosions rapidly create a region with a large energy density near the surface of a planet. Once this energy is deposited, the subsequent expansion of the shock wave is similar in both cases. The kinetic energy of an impactor of mass m and velocity v, $1/2mv^2$, is approximately equivalent to the explosion energy W (Melosh, 1989). The body force system for an explosion source is equivalent to a moment tensor with equal non-zero diagonal terms.

The moment tensor is time dependent and is often written as

$$M(t) = M_0 x(t) \ , \tag{1}$$

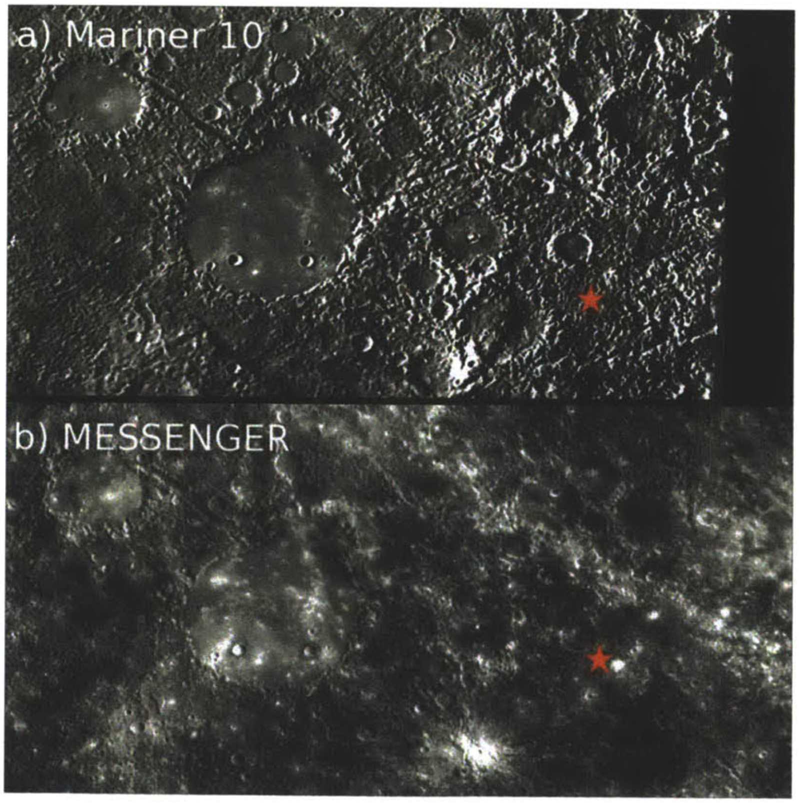

Fig. 2. Images of the hilly and lineated terrain at the antipode of the Caloris basin from Mariner 10 and MESSENGER. The location of the antipode to the center of the Caloris basin is marked by red stars (Solomon et al., 2001; Murchie et al., 2008). The large, smooth-floored crater just left of center is 150 kilometers in diameter. Credit: NASA/Johns Hopkins University Applied Physics Laboratory/Carnegie Institution of Washington. (http://messenger.jhuapl.edu)

where M_0 is a scale factor and $x(t)$ is the source time function. The source time often investigated in the frequency domain. To describe the source spectrum (Fig. 3) we used a single corner frequency approximation. The spectral range is from low frequencies close to 0 to the corner frequency (Stein and Wysession, 2003). We can characterize the explosion source model for a meteoritic impact with three parameters: scalar moment M_0, corner frequency f_c , and depth of burial H. We must then choose appropriate values of these parameters for the Caloris impact. The traditional approach to characterization of large impacts is to extrapolate beyond experimental knowledge by means of scaling laws. The average impact velocities on Mercury are approximately 40 km/s (Schultz, 1988). At this velocity, crater scaling relationships (Holsapple, 1993) constrain the projectile to have been approximately 100 km in diameter. Assuming the density of the impactor to be 3000 kg/m^3, the kinetic energy of the Caloris impactor is of the order of 10^{27} J. For comparison, the energy of the largest nuclear explosion is at the order of 10^{17} J (50,000 kt) and most nuclear explosions are below 1000 kt. For another comparison, the radiated energy as elastic seismic waves of the Sumatra earthquake was of the order 10^{17} J as well. The magnitude of the Caloris impact event is many orders (over 10^{10}) higher than the magnitude range of experimental knowledge, and consequently extrapolation using scaling laws from nuclear explosion tests and earthquake studies will be risky, and should be regarded with caution. Furthermore, it is common to encounter uncertainties up to orders of magnitude with scaling laws in impact cratering studies. The uncertainty remains high in part because the equation applies to the transient cavity, which is difficult to assess for actual craters observed on planetary surfaces (Watts et al., 1991). Due to the depth of burial H for impact, studies on the Meteor Crater, Arizona, estimated the value varying from less than the diameter to 4-5 times of the diameter of the projectile (Melosh, 1989). Melosh (1989) suggests that the equivalent depth of burial H for an impact may be roughly estimated from the classic jet-penetration formula

$$H = L\left(\frac{\rho_p}{\rho_t}\right)^{1/2}, \tag{2}$$

where L is the projectile diameter, ρ_p is its density and ρ_t is the target density. Based on these approximations, the parameters of the explosion source in this study are only loosely constrained by scaling laws and experimental knowledge from smaller impactors, nuclear explosion tests and large earthquakes. We discuss the plausible range and sensitivity of these parameters to the antipodal magnitude of seismic waves below.

2.2. Seismic wave propagation through Mercury

Early thermal evolution models of Mercury indicated that an initially molten core should have frozen out by now (Siegfried and Solomon, 1974; Cassen et al., 1976; Fricker et al., 1976) unless a light element such as sulfur is present (e.g., Sanloup et al., 2002); sulfur can considerably lower the melting temperature of iron at high pressure (Fei et al., 2000). While a core composition with the sulfur content required to maintain a fluid state (~0.1 weight percent (Schubert et al., 1988)) is challenging to reconcile with solar system condensation models (Lewis, 1972) unless there has been input from material at heliocentric distances beyond Mercury, evidence favors a core that is currently at least partially molten. Mercury's dipole magnetic field (Connerney and Ness, 1988; Purucker et al., 2009; Uno et al., 2009) and observations of the planet's low-degree gravity field (Anderson et al., 1987) coupled with the

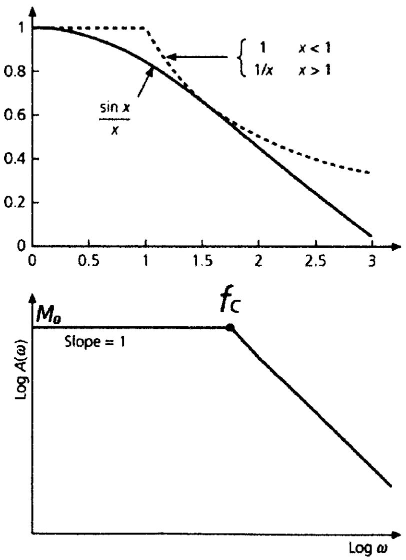

Fig. 3. Top: Approximation to the function $\sin(x)/x$ used in modeling the source spectrum. Bottom: a common approximation uses a single corner frequency f_c. The flat segment extending to zero frequency gives M_0. (Stein and Wysession, 2003).

obliquity and forced physical libration (Margot et al., 2007) indicate that at least Mercury's core is partially molten at present, although the ratio of molten to solid core material is not yet constrained. In this analysis we construct models of the early internal state of Mercury varying from a totally solid core to a fully molten core. Given the current internal state (Margot et al., 2007), it is certain that at the time of the Caloris impact the core must have been largely molten; a solid inner core would have been rather small if it existed at all. Although the model with a totally solid core is not plausible at the time of impact, it is useful to consider as an end member in the sense that it provides an indication of the sensitivity of the propagation to core state.

2.2.1. 1-D Seismic Structure of Mercury

Owing to advances in thermodynamic modeling and improved knowledge of the shear properties of Earth and mantle minerals at high temperature and pressure from mineral physics, it is now possible to compute, in a self-consistent manner, both bulk and shear properties for silicate compositions (e.g., Stixrude and Lithgow-Bertelloni, 2005). Furthermore, due to the relatively low pressure of Mercury's interior, extrapolation to high pressure for both elastic and anelastic properties, which is a significant source of uncertainty for the Earth's mantle (e.g., Cammarano et al., 2006), is less problematic for Mercury. The uncompressed density (5017 kg/m^3) of Mercury suggests that if the planet differentiated into a silicate mantle and metallic core, then the core radius R_{core} is about 75% of the planet radius R_{planet} and the fractional core mass is about 0.65 (Siegfried and Solomon, 1974). Details of the core composition are unclear (Zuber et al., 2007), although iron is widely agreed to be the dominant element. We assume that Mercury has an iron-nickel alloy core containing 10% nickel by weight, which is a rough average of the Ni concentration in stony-iron meteorites (Siegfried and Solomon, 1974). For the molten case, 10% sulfur has been incorporated into the core. The Fe-S system has been studied extensively and physical properties of Fe/FeS have been determined are generally the same except for density. Therefore, in our modeling we only account for the density

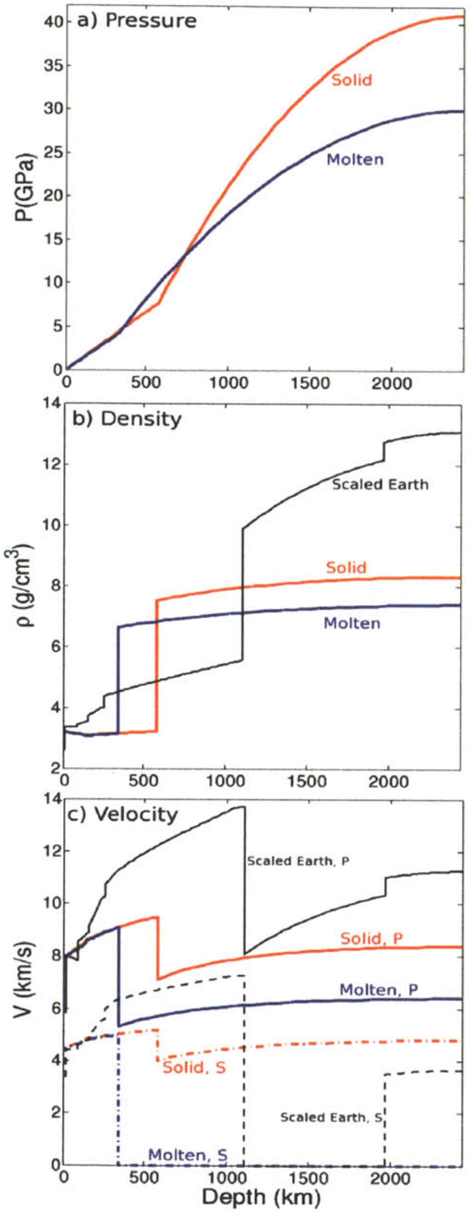

Fig. 4. Two end-member physically consistent 1-D seismic structure models of Mercury. The blue curves show the property profiles for a model with a molten core; the red curves are for a model with a solid core. The thin black curves are profiles of PREM scaled to Mercury. In c), the solid curves show P wave velocities, and the dashed or dot-dashed curves show S wave velocities.

effect of nickel. After calculating the average density of Fe10%Ni alloy, we treat the Fe-Ni alloy as Fe afterward. Due to scarcity of data, the crust and the details of mantle structure are not accounted for in this study. Two main chemically homogeneous layers are considered: the silicate mantle, and the metallic core. Note that there are no phase transitions in the mantle, because of the relatively shallow mantle of Mercury (< 600 km) and consequently low pressure (< 8 GPa) (Fig. 4a). Pressure as a function of depth is relatively well constrained. The pressure gradient in the mantle of Mercury is close to 0.013 GPa/km (Basaltic Volcanism Study Project, 1981) and pressure is assumed to be hydrostatic in the core. The pressure at the core-mantle boundary (CMB) changes with the depth of the CMB and the pressure at the center of the planet also changes with the depth of the CMB and the core composition (Fig. 4a). The surface temperature is taken to be 440 K, the mean temperature of Mercury's surface (Harder and Schubert, 2001). Based on a recent evolution model of Mercury (Hauck et al., 2004), at the time of the impact event the temperature is about 1750 K at the base of the thermal lithosphere and is about 1825 K at the CMB. The temperature distributions are taken to be adiabatic in the mantle and core, respectively (Harder, 1998). Thermodynamic properties as a function of pressure and temperature are computed for each layer using equations of state based on the most recent mineral physics data. We followed the procedure described in Duffy and Anderson (1989). The calculated density profiles for two models are shown in Fig. 4b. The Preliminary Reference Earth Model (PREM) (Dziewonski and Anderson, 1981) scaled to Mercury's radius is plotted for comparison. The depth of the core-mantle boundary is constrained by the mass and core composition for each physical model. Figure 4c shows the *P* and *S* wave velocities of two end-member models. The rate of increase with depth of the *P* and *S* wave velocities is considerably smaller than in the Earth because of the lower rate of increase of pressure with depth due to the smaller planetary mass.

2.2.2. Seismic wave attenuation

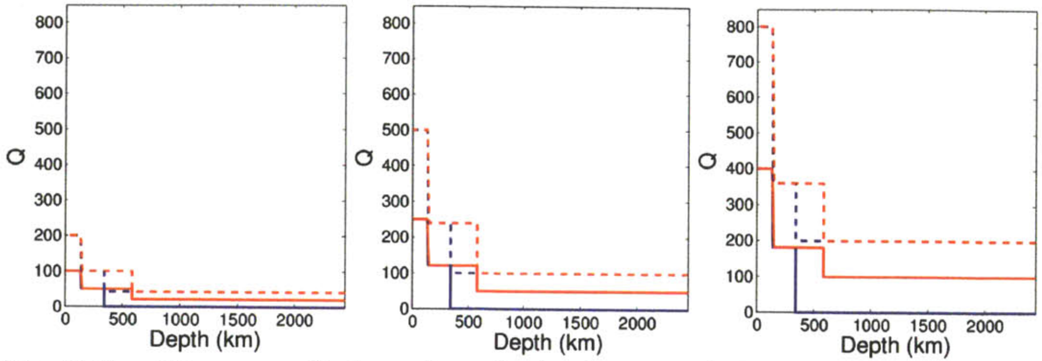

Fig. 5. Possible range of attenuation of seismic waves in Mercury. Parameters Q_α (dashed lines) and Q_β (solid lines) control the attenuation of *P* and *S* waves, respectively. Blue, model with molten core; red, model with solid core. Right: lower-bound model with least attenuation (higher *Q* values), which is similar to Earth. Center: one optimized model. Left: upper-bound model with most attenuation (lower *Q* values).

Knowledge of the anelastic structure of Mercury is essential to accurately characterize the seismic waves that propagate through the planet. A quality factor *Q* is usually used to describe the attenuation of seismic waves, and Q_α and Q_β control the attenuation of *P* and *S* waves, respectively. Figure 5 shows the attenuation models we used in this work. Since early Mercury was probably much hotter than the current Earth, we use the attenuation profile of PREM Earth model as the lower bound model with least attenuation.

2.2.3. Body and surface waves in Mercury

The impact generates seismic waves. Due to its unique structure, wave propagation in Mercury is different from that within the Earth. We first investigate the propagation problem using a point explosion source under the assumption that the seismic source is small and the resultant strain is within the linear elasticity range. In addition to the propagation, we also consider several aspects related to the source: the scaling and cutoff frequency of the source spectrum and the effect of finite source area. We used three different methods to simulate seismic wave propagation in spherical Mercury: the normal mode summation code MINEOS1.0 (http://www.geodynamics.org), the 3-D spectral element method (SEM) (e.g., Komatitsch *et al.*, 2000), and the direct solution method

(DSM) (Geller and Ohminato, 1994; Kaiwa *et al.*, 2006). All these methods produced the same results. It is known that the Mineos code is not suitable for computing high-frequency (~>0.2 Hz) wave propagation due to its interpolation method. However, based on the source scaling law (e.g., Gudkova *et al.* 2011), large events are usually associated with large source areas and produce relatively more low-frequency waves than high-frequency waves. So it is appropriate to use Mineos to study a large impact. For a small impact, the source spectrum is wide and we need a method that can simulate high-frequency wave propagation. The DSM is a good choice. We have also modified the original DSM, which can only handle point double-couple sources, to handle an impact with a finite area. The DSM is a frequency-domain method and our computational andwidth is from 0 Hz to at least 0.5 Hz, which is sufficiently high to account for both body and surface waves and to study the effect of different source cutoff frequencies.

The proposed molten-core model has a thin but high-velocity (V_p) mantle overlying a low velocity core. To understand the body wave propagation, we traced seismic rays in Mercury (Fig. 6). The direct *P* wave travels in the mantle for epicentral distances of up to ~47.7°. Due to the velocity drop in the core, there is a shadow zone in the distance range of 47.7°-121° within which no direct seismic rays can arrive. However, seismic waves are not optical rays and they have finite wavelengths. In this case, the curved CMB diffracts the *P* wave into the shadow zone. From 121° to 129°, there are two *PKP* arrivals: *PKP-ab*, a reverse branch, which arrives at shorter distances as the ray becomes steeper due to the curvature of the CMB; and the *PKP-bc* branch, extending all the way to the 180° antipode and arriving earlier than *PKP-ab*. Seismic rays for *S* waves in the mantle are similar to those of the *P* waves because the V_p/V_S ratio is almost constant in the mantle. No shear wave penetrates the liquid core. An interesting feature to note is that on Mercury, *PKP* is not necessarily the earliest arrival, as multiple *PcP* (or *PcPn*, meaning a downgoing *P* wave that has been reflected at the CMB *n* times and at the surface *n*-1 times) can arrive earlier than *PKP* (Fig. 7).

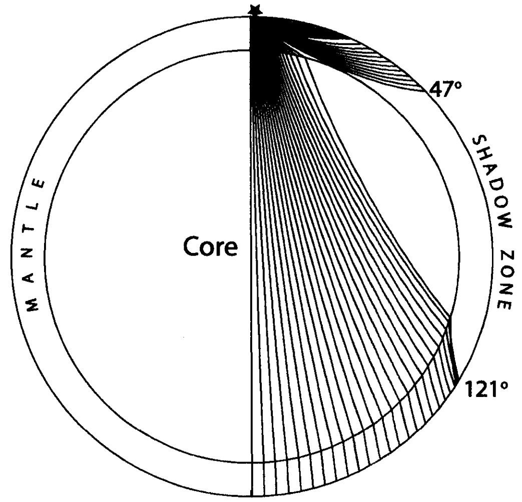

Figure 6. Seismic ray paths for the direct *P* wave, which travels in the mantle, and for the core phase *PKP*. The source is at the surface.

We discovered a train of large-amplitude waves that arrive earlier than the Rayleigh wave in the antipodal region (Fig. 7a & b). These waves are mantle-trapped body waves and their large amplitudes are due to interference of multiple *PcP* and *PcS* waves within Mercury's thin mantle. On the Earth, the compressional impedance contrast across the CMB is almost constant (< 5% contrast). As such, the *P* wave reflection off the CMB is very weak at close distances. However, this is not the case for Mercury. For a vertically incident *P* wave, the impedance contrast across Mercury's CMB is large at ~20%. Note that the reflection coefficient increases as the incidence angle increases. So for an obliquely incident wave the reflection coefficient can be much larger than 0.2. With a thin mantle and *P*-to-*SV* conversions, multiple reverberations of *P* and *S* waves between the surface and the CMB develop strong mantle trapped waves. Contrary to the common mechanism for trapping waves, which involves a low-velocity layer on top of a high-velocity region, on Mercury, the trapping is mainly provided by the large density contrast between the thin mantle and the core. For surface waves, due to the symmetry of the problem, only Rayleigh (no Love) waves exist. Because a fast mantle overlies a slow core, the dispersion characteristic is opposite to that on the Earth and, for Mercury, the high-frequency Rayleigh wave propagates faster than the low-frequency wave. And also because the mantle is thin, only short- and intermediate-period Rayleigh waves propagate relatively unattenuated. Long-period Rayleigh waves leak energy into the core and thus attenuate rapidly.

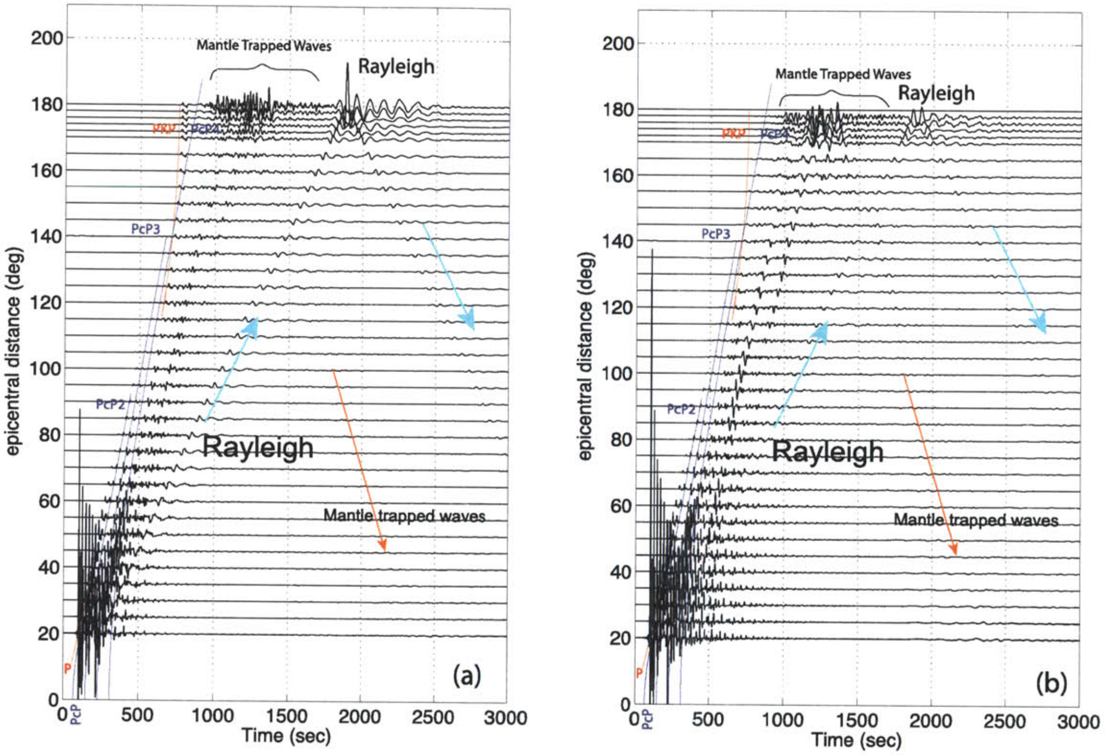

Fig. 7. Vertical (a) and radial (b) displacements computed using the DSM at different angular distances from the source. The seismic source is a moment magnitude M_W 6 event. The corner frequency $f_c = 0.1$ Hz, the source spectrum follows ω^1-type scaling, and the depth of burial $H =$ 100 km. The high end of the frequency bandwidth in the computation is 1 Hz and the final seismograms are bandpass filtered between 0.001 Hz and 0.5 Hz. The red lines are *P* and *PKP* wave travel-time curves predicted by ray tracing.

For both the mantle trapped waves and the surface Rayleigh waves, the seismic energy builds up drastically as the waves approach the antipode and both waves have comparable amplitudes (Fig. 7). Due to Mercury's peculiar seismic structure, the mantle-trapped waves may be identified as a new and important mechanism for the antipodal disruption. As the mantle trapped waves travel much faster than the Rayleigh waves, they produce the first significant surface disruption around the antipode, followed by a second disruption by the Rayleigh waves.

2.2.4 Various source effects

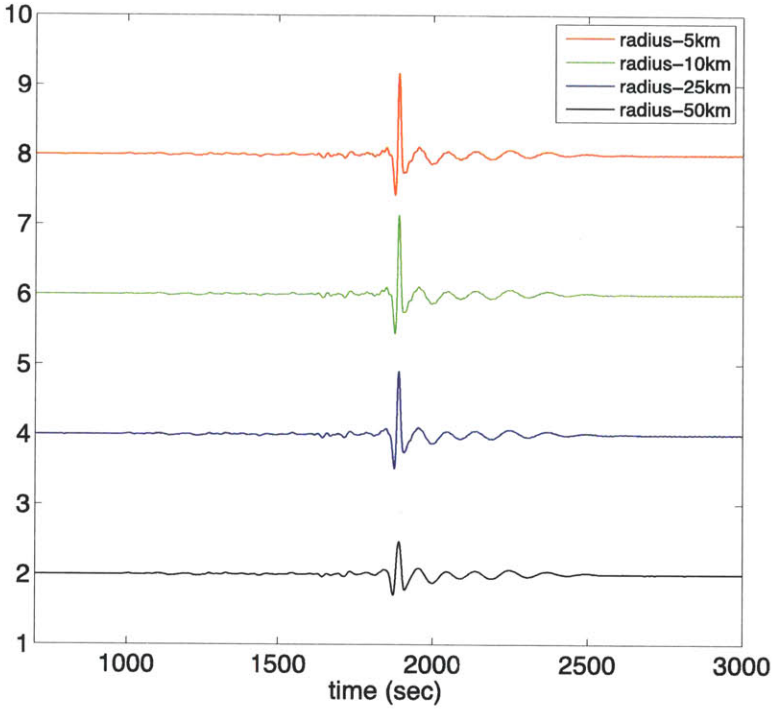

Fig. 8. Vertical displacements (normalized by source area) at the antipodal point (i.e., epicentral distance 180 degrees) for different area sources. We assume the area source is circular and the force direction is vertical. The source depth is at 10 km. The computational bandwidth is between 0 and 0.5 Hz and the final result is filtered between 0.001 Hz and 0.1 Hz.

Thus far, the impact is approximated as a point explosion source. Our purpose has been to understand propagation effects due to the Mercury seismic velocity structure. However, the impact is not a point and it has a finite size, which stimulates us to look into the effect of the finite source area. To do this, we follow the approach used by Takeuchi and Saito (1972) in the study of surface wave generation, which treated the source as a traction discontinuity. We assume that the impact is a vertical area force with a radius R_s and it is at 10 km depth. Assuming constant force per unit area, we computed the seismograms for several different source areas (Fig. 8). We observed that for the shallow source, the Rayleigh wave dominates. As we increase the source area, the high-frequency content is gradually suppressed; the whole spectrum shifts to the low end and the maximum wave amplitude decreases by about a factor of two.

It has been recognized that different source spectral scaling relations beyond the cutoff frequency might exist for a celestial impact (Gudkova et al., 2011) other than the ω^1-type scaling. Note that here ω^1 is for the source spectral amplitude, not the power, which scales as the square of the spectral amplitude: ω^2. We tested two different scaling relations, ω^1 and ω^2, for the source spectral amplitude. For the ω^2 law, the high-frequency content is less than for the ω^1 law. However, for the same cutoff frequency, the difference in amplitude is not significant between the two different scalings (Fig. 11). The cutoff frequency may have a large effect on the displacement (factor of ~2 for the Rayleigh waves or factor of 5 for the body waves) when the cutoff frequency is very low (Fig. 9). So, roughly speaking, the various aspects of the source, including the effect of finite source area, the cutoff frequency and different source scaling relations, can change the antipodal displacement only by a factor of less than 10.

The capability of generating surface waves depends on the source depth. We also computed the antipodal displacement for a point explosion source at different depths (Fig. 10). As one expects, the surface Rayleigh wave amplitude decreases as the source depth increases. In fact, the mantle trapped waves have about the sampe amplitude across all cases and, because of their high frequencies, mantle trapped body waves can induce similar tensile stresses as the Rayleigh wave.

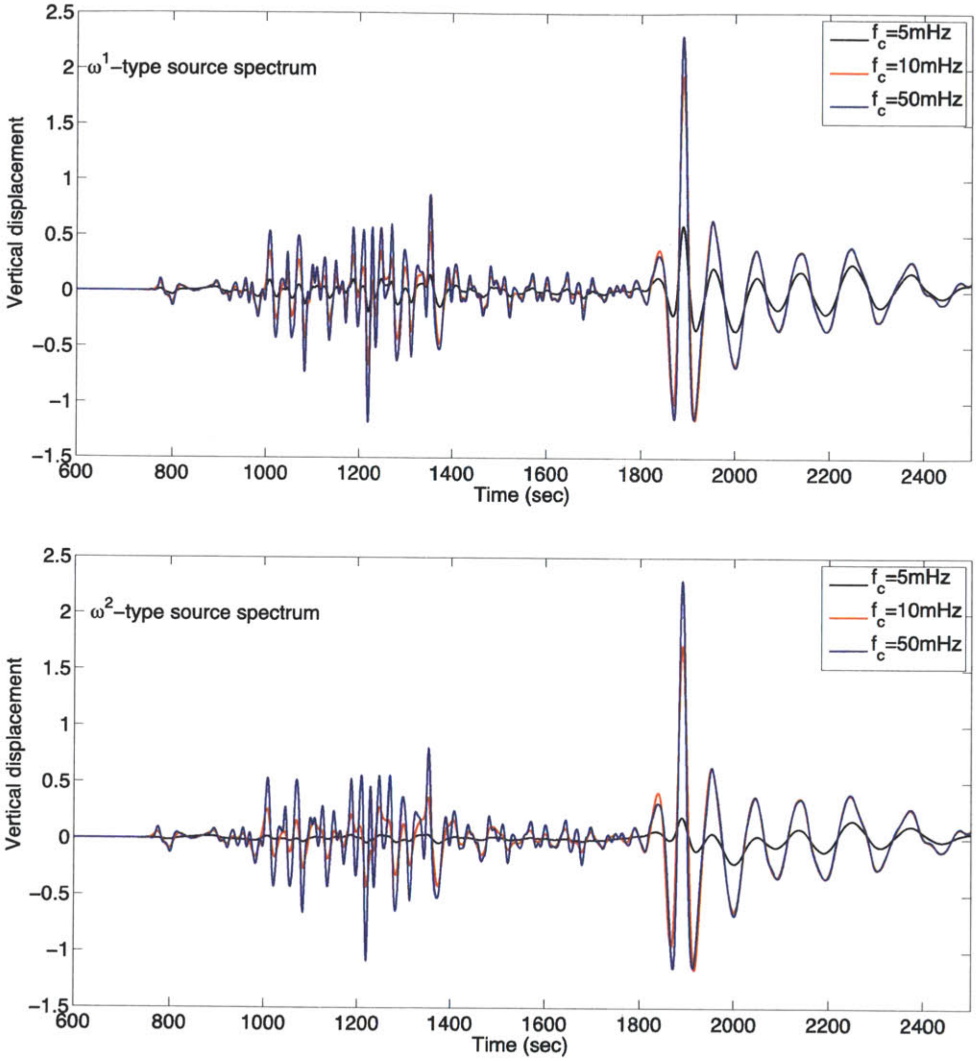

Fig. 9. The effect of different scaling laws, ω^1- and ω^2 -type, for the source amplitude spectrum and different cutoff frequencies (f_c) on the antipodal seismogram produced by a point explosion at 100 km depth. We did not plot the case f_c=100 mHz because the waveform is same as f_c=50 mHz. The computational bandwidth is between 0 and 1 Hz.

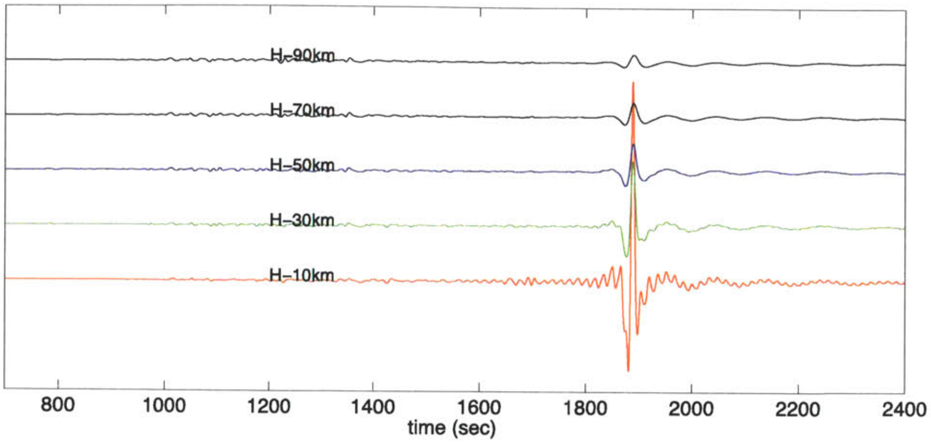

Fig. 10. Antipodal seismograms for different source depths, *H*. The amplitudes are relative. In this example, the double-couple time history is a delta function and the resultant displacement is bandpass filtered between 0.001 Hz and 0.1 Hz. The source is a point explosion and the cutoff frequency f_c is 0.1 Hz of the ω^1 type.

2.3 The Caloris impact and antipodal disruption

We calculate several models with large sources consistent with the size of the Caloris basin. The purpose of these calculations is to determine quantitatively the stresses and the displacements at the antipode and the disrupted region.

It is important to mention that the calculations for large sources make some major approximations and the results should be evaluated with these limitations. First, we use linear elasticity and the associated wave equation even though the displacements and strains are large. We partially compensated for the effect by using high attenuation. The second approximation is we use the moment tensor representation for the source. In reality, the generation of seismic waves by a large impact requires a hydrodynamic code. As waves propagate farther from the source, these effects decrease.

We use the normal mode summation code to carry out the simulation of synthetic seismograms. First, we calculate the normal modes for both end-member models of

Mercury's 1-D seismic structure. All modes are computed with frequencies less than 0.167 Hz (or periods greater than 6 s) to accommodate the body wave signals. Boslough et al. (1996) used modes with periods greater than 45 s, which led to loss of the major body wave signals in the synthetic seismograms. We then generate synthetic displacement, strain and stress time histories at different angular distances from the source. Because of large uncertainties on seismic source parameters, we run a group of models with variable source parameters. Figure 11 shows the displacement histories at different angular distances from the source for one example model. Small variations in seismograms between this model and those shown in Fig. 7 are due to the difference in the source and velocity models used. For simplicity, in our models we assume the

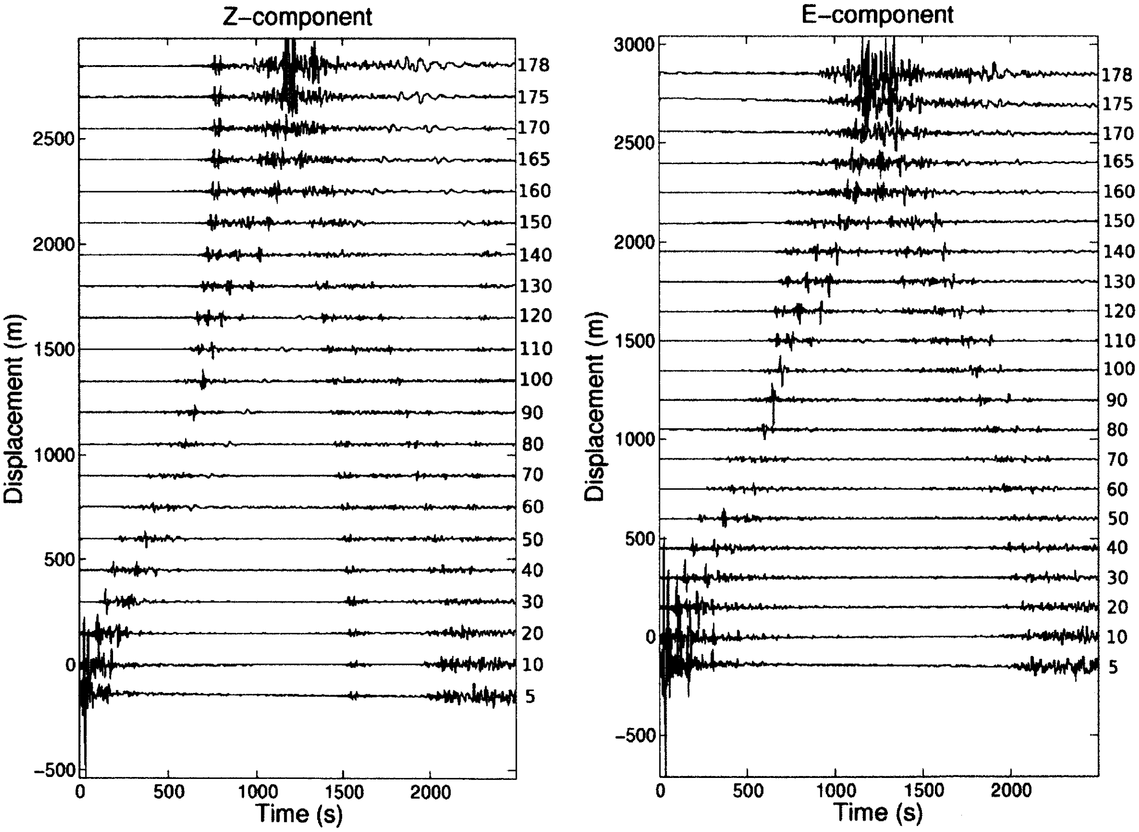

Fig. 11. Displacement histories determined by normal mode summation at different angular distances from the source. The angular distances are marked at the right side of the seismograms (from 5 to 178°). The seismic source parameters used for this model include: scalar moment

$M_0 = 0.86 \quad 10^{34}$ dyne-cm, corner frequency $f_c = 100$ mHz, depth of burial $H = 100$ km.

explosion source is on the equator of Mercury and all the receivers are on the equator as well, so the displacements are mainly in the vertical and east-west directions (Z-component and E-component in Fig. 11). Figure 12 shows the displacements and principal stress histories at the angular distance of 175° for the same example model.

The dynamic stresses due to focused seismic waves lead to antipodal disruption. To explore the relationship between the seismic waves and antipodal disruption, we first quantitatively characterize the first-order feature of the disrupted terrain. Approximating the disruption zone as circular, the antipodal disrupted terrain with an area of at least 500,000 km^2 (Murray et al., 1974) corresponds to about 400 km (or 9 angular degrees) in radius. The height scale of the hills and depressions is up to about 2 km (Murray et al., 1974). The tensile strength is substantially lower than the compressive strength of rocks and the typical tensile strength of intact rock is about 20 MPa (Jaeger and Cook, 1979). We assume a tensile strength of crustal materials is 10 MPa. Because of the large height scale of the disruption features, we assume that the disruption penetrated at least to a depth of 1 km. The static stress at 1 km depth is about 13 MPa. Therefore the peak amplitude of dynamic stresses needs to exceed 33 MPa to induce rupture, and we used this as the critical value of the rupture stress.

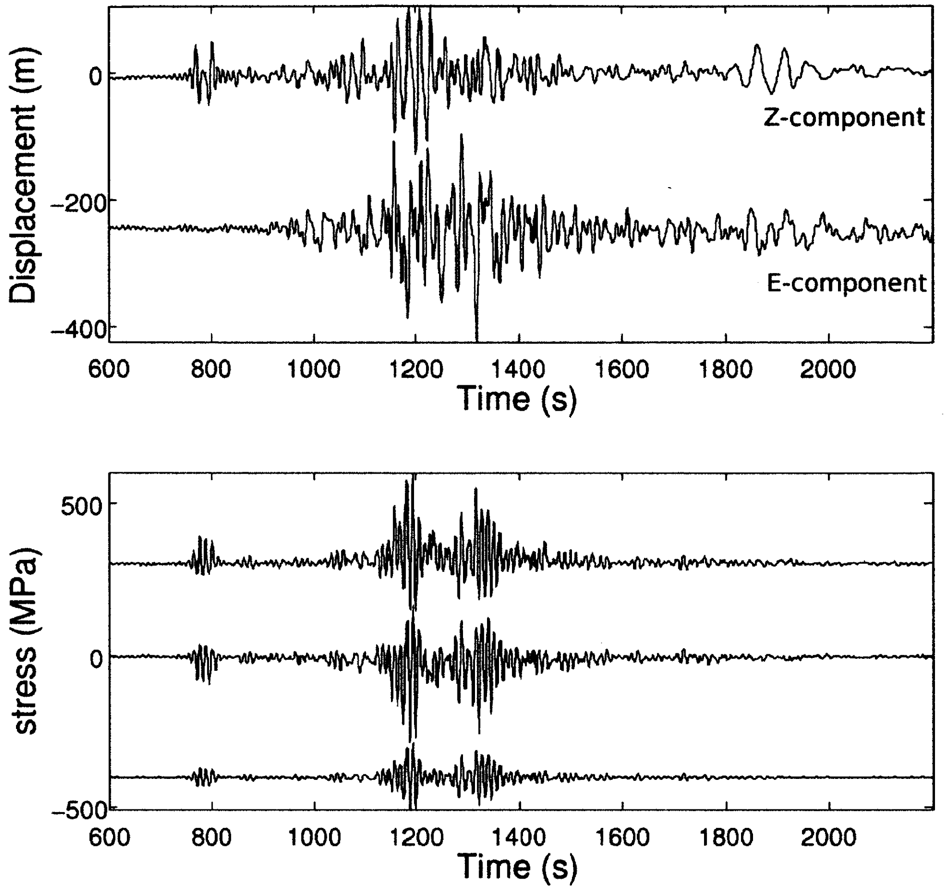

Fig. 12. Displacements and principal stresses at an angular distance of 5° (215 km) from the antipode. The source parameters and internal state model are the same as Fig. 6. The peak amplitude of displacement is about 150 m; the peak amplitude of stress is about 250 MPa.

Chapter 3

Results and discussion

3.1. Role of internal state

We next explore the effects of source model parameters and internal state on the antipodal seismic waves. The peak stress of the seismic waves is modulated by both the source model and the internal state model. A series of models has been calculated with the depth of burial H varying from 20 to 100 km and with the corner frequency f_c varying from 50 to 100 mHz. Figure 13 shows the calculated static moment M_0 for models with source parameters and internal state models selected to generate critical peak stress within 5 angular degrees from the antipode. Each pair of markers with a connecting bar represents one model with a certain source and internal structure model (Figs. 4 and 5). The lower value of each pair is calculated to generate the critical peak stress precisely at the antipode. The higher value of each pair is calculated to generate the same stress at location 5 angular degrees away from the antipode. The models marked as circles have a solid core, whereas models marked as squares have a molten core. We can see that the ranges of the magnitude of static moment are almost identical for models with both solid and molten cores. The results demonstrate that the planetary internal structure has limited effect on the peak magnitude of the seismic response of the impact.

The partitioning of energy among different seismic modes (surface and body waves) is affected by the seismic source models. Surface waves tend to dominate when models are characterized by a relatively shallower source and lower corner frequency, whereas body waves tend to dominate when models are characterized by a relatively deeper source and higher corner frequency. In Fig. 13, models marked in red are dominated by surface waves, and models marked in blue are dominated by body waves. The seismic response appears more sensitive to the source models than the core state.

To cause surface rupture at the antipode, the magnitudes of M_0 are generally on the order of 10^{33} dyne-cm or 10^{26} Nm, and if we convert the scalar moments to moment magnitudes, the corresponding M_W is about 12. For comparison, the scalar moment for the 2004 Sumatra earthquake is about 10^{30} dyne-cm or 10^{23} Nm (Kanamori, 2006). The radiated energy of the Sumatra earthquake was about 3 10^{17} J, so the energy-moment ratio is about 10^{-5} (Kanamori, 2006). If the explosion source has a similar energy-moment ratio, then the energy radiated as seismic waves from the impact was of the order 10^{22} J. The initial kinetic energy of the impactor is estimated to be of order 10^{27} J, so the ratio of radiated seismic energy to the impactor kinetic energy (sometimes called the seismic efficiency factor) is about 10^{-5}. Previous studies on much smaller-scale impactors estimated the seismic efficiency factor at 10^{-6} to 10^{-2} (McGarr et al., 1969; Latham et al., 1970b,a).

3.2. Role of antipodal seismic focusing

Figure 14 shows the variation of peak stress amplitudes with angular distance from the source. The first-order feature of the curves is that the amplitudes decrease rapidly away from the antipode, within about 2-3 angular degrees, and the amplitudes change little after about 5 angular degrees away from the antipode. The greatest stresses occur within about 5 angular degrees of the antipode (Fig. 14). Our results show that the peak stress amplitudes versus angular distance is a relatively robust result, because it is not significantly affected by either the source parameters or the internal state. The images of chaotic terrain on Mercury show that the disruption zone had a somewhat irregular shape and larger radius (5-9 angular degrees). We suggest that mantle guided waves and surface

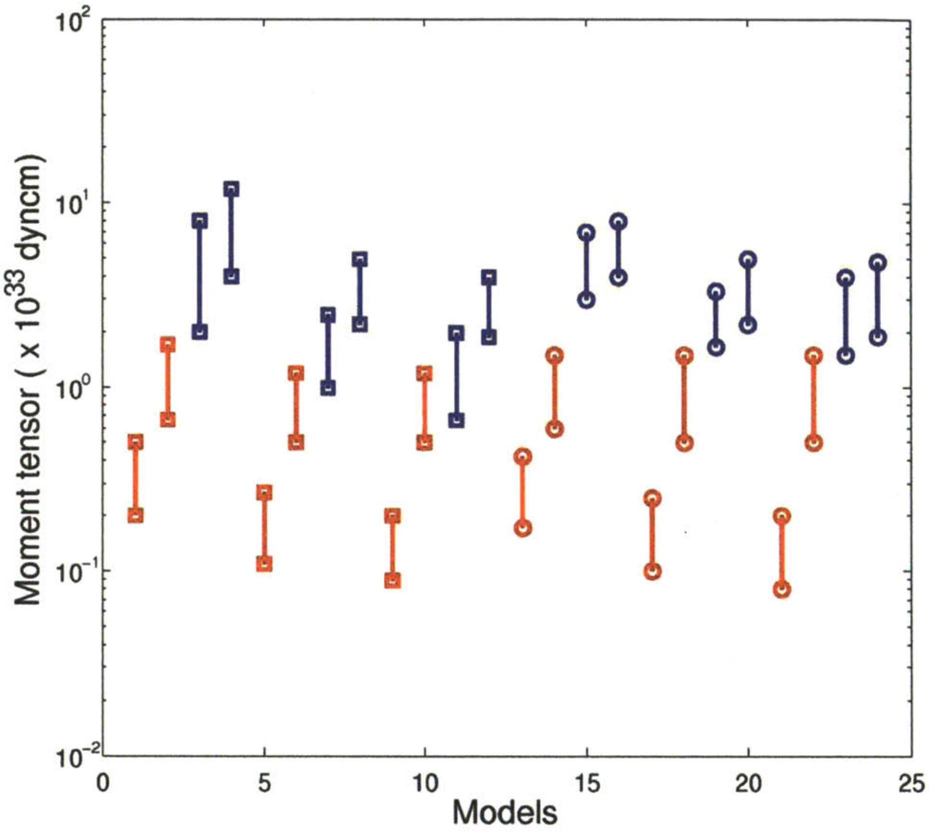

Fig. 13. Range of static moment M_0 for different models that produce the same surface disruption. Surface waves dominate for the group of models in red; body waves dominate for models in blue. Models marked as circles have a solid core; models marked as squares have a molten core.

waves modulated by (unmodeled) shallow structure may have influenced the nature of the disruption zone.

3.3. Comparison with previous studies

Previous studies have addressed the formation of disrupted terrains antipodal to major impacts in general (Watts et al., 1991) and to the Caloris impact on Mercury in particular (Schultz and Gault, 1975; Hughes et al., 1977; Watts et al., 1991). Our study utilizes 1-D internal structure models of Mercury to investigate the relevance of Mercury's internal state, with emphasis on the core, and the antipodal seismic response to the Caloris impact.

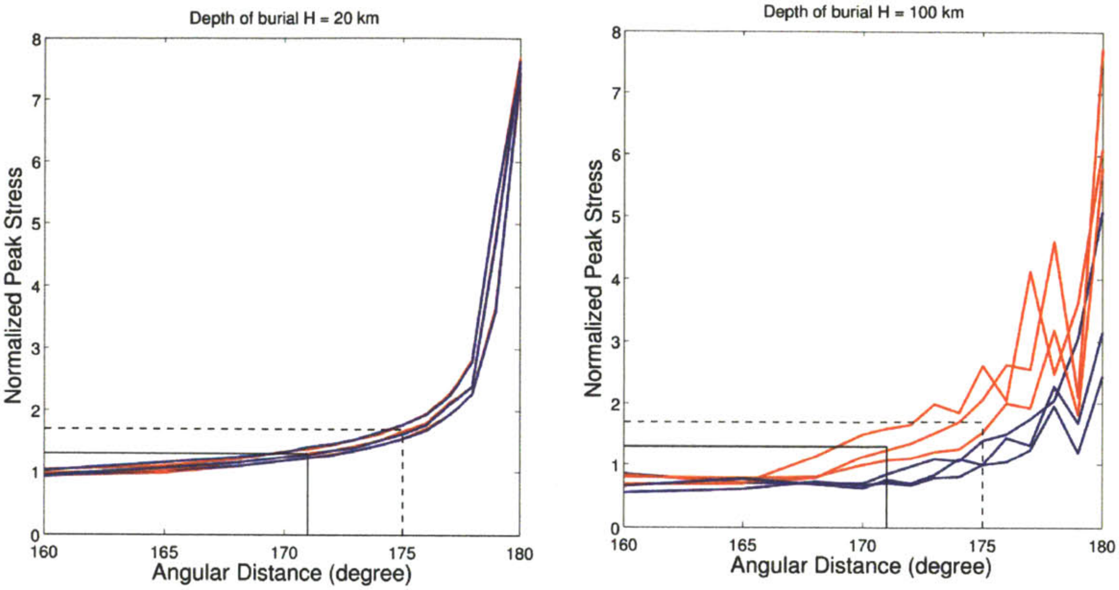

Fig. 14. Variation of peak stress with angular distance from the antipode, located at the right side of each plot (180° of angular distance from the source). Each model is normalized by the value at the angular distance of 135°. The two groups of models shown here have different depths of the equivalent explosion source. (a) 20 km deep source, for which surface waves dominate. (b) 100 km deep source, for which body waves dominate. Blue and red curves are models with molten and solid cores, respectively.

The goal is to quantify how the internal state affects the seismic response at the antipode of a major impact. We seek to understand whether it is possible to constrain internal models on the basis of the nature of impact-generated antipodal disruption. Internal structure models used in previous studies were more simplified, usually with uniform density, ignoring the gradual increase of properties with depth. Hughes et al. (1977) underestimated the radius of Mercury (2000 km instead of ~2440 km), and ignored the discontinuity in velocity between the mantle and core. We note that the objective of the previous studies was to evaluate whether it was feasible for the Caloris impact to generate the antipodal disruption, but they did not address the details of the disruption zone. In this study the internal structure models that we employ are constructed in a self-consistent way, accommodating the gradual changes of material properties with depth and the discontinuity of the core-mantle boundary, owing to advances in thermodynamical modeling and mineral physics. Although because of uncertainties in the composition and temperature profile a wide range of possible models is allowable, our model captures the first-order features in each case. The most uncertain aspect of the investigation is the characterization of the impact source. Previous studies basically treated the seismic wave as a single saw-toothed wave (Schultz and Gault, 1975) and assumed that a fraction of the projectile's kinetic energy was imparted to radiated seismic waves (Schultz and Gault, 1975; Hughes et al., 1977; Watts et al., 1991; Williams and Greeley, 1994). The actual form of the seismic waves is typically a series of complex oscillatory ground motions resulting from wave dispersion. In contrast to previous studies, we used a two-step modeling approach, as was used to study the possible link between flood basalts and hotspots on Earth (Boslough et al., 1996). Two separate modeling steps are required to evaluate the source and propagation because of the wide variation in spatial and temporal scales. We model the source as an explosion source with three parameters derived from knowledge of nuclear explosions and large earthquakes on Earth. Combining with normal mode summation, we are able to characterize the energy partitioning between various seismic modes. Our modeling results demonstrate that the antipodal seismic response is more sensitive to the equivalent source function models of the Caloris impact than to Mercury's core state. Moreover, the sensitivity of the seismic response to internal state is dependent on the dominant seismic modes. Both the source function of the impact and the internal state models are required to obtain a reasonable estimation of the seismic response at the antipode.

Chapter 4

Summary and conclusions

We have constructed two end-member 1-D seismic structure models of Mercury. Because the core appears to be at least partially molten at present (Margot et al., 2007), it was, in all likelihood, fully or mostly molten at the time of the Caloris impact. There is little effect on the modeling results if a rather small inner solid core was present instead of a fully molten core. The seismic response at the antipode to the impact is affected not only by the planet's internal state, but also depends on the equivalent source function of the impact. We have elucidated how the sensitivity of antipodal seismic response to the internal state is dependent on the dominant seismic modes. We find that the effects of internal state on the antipodal seismic response is not significant compared to the uncertainty level of the equivalent source function of impact. We also find that the distribution of peak stress with angular distance is not significantly affected by the source parameters and internal state models (Fig. 14). The first-order feature of the peak stress distribution is that the amplitude decreases rapidly away from the antipode within about 5 angular degrees. For the models we have investigated a disruption zone about 5 angular degrees in radius is most probable. From the observed antipodal disruption on Mercury, the radius of the disruption zone is 5-9 angular degrees.

A likely scenario for the creation of the disrupted terrain is a combination of two effects: (1) guided mantle waves, with high frequencies and stresses that fracture crustal materials; and (2) later Rayleigh waves, which produce large vertical displacements and help move and disaggregate the fractured blocks. More detailed modeling of Mercury's shallow internal structure, which will be elucidated once the MESSENGER spacecraft enters orbit about Mercury (Zuber et al., 2007), will help us to understand its possible influence on the structure of the antipodal disruption zone.

Bibliography

Anderson, J.D., Colombo, G., Esposito, P.B., Lau, E.L., Trager, G. B., 1987. The mass, gravity field, and ephemeris of Mercury. Icarus 71, 337–349.

Basaltic Volcanism Study Project, 1981. Basaltic Volcanism on the Terrestrial Planets. Pergamon Press, New York, 1286 pp.

Boslough, M.B., Chael, E.P., Trucano, T.G., Crawford, D.A., Campbell, D.L., 1996. Axial focusing of impact energy in the earth's interior: a possible link to flood basalts and hotspots. In: Ryder, G., Fastovsky, D, Gartner, S. (Eds.), The Cretaceous–Tertiary Event and Other Catastrophes in Earth History. Special Paper 307, Geological Society of America, Boulder, Colo., pp. 541–550.

Cammarano, F., Lekic, V., Manga, M., Panning, M., Romanowicz, B., 2006. Long-period seismology on Europa: 1. physically consistent interior models. J. Geophys. Res. 111, E12009, doi:10.1029/2006JE002710.

Cassen, P., Young, R.E., Schubert, G., Reynolds, R.T., 1976. Implications of an internal dynamo for the thermal history of Mercury. Icarus 28, 501–508.

Connerney, J.E.P., Ness, N.F., 1988. Mercury's magnetic field and interior. In: F. Vilas, C.R. Chapman, M.S. Matthews (Eds.), Mercury. University of Arizona Press, Tucson, Ariz., pp. 494–513.

Duffy, T.S., Anderson, D.L., 1989. Seismic velocities in mantle minerals and the mineralogy of the upper mantle. J. Geophys. Res. 94, 1895–1912.

Dziewonski, A.M., Anderson, D.L., 1981. Preliminary reference Earth model. Phys. Earth Planet. Inter. 25, 297–356.

Fei, Y., 1995. Thermal expansion. In: Ahrens, T.J. (Ed.), Mineral Physics and Crystallography: A Handbook of Physical Constants. AGU Reference Shelf, vol.2. American Geophysical Union, Washington, D.C., pp. 29–44.

Fei, Y., Li, J., Berka, C.M., Prewitt, C.T., 2000. Structure type and bulk modulus of Fe_3S_2, a new iron-sulfur compound. Amer. Mineral. 85, 1830–1833.

Fricker, P.E., Reynolds, R.T., Summers, A.L., Cassen, P.M., 1976. Does Mercury have a molten core? Nature 259, 293–294.

Geller, R.J., Ohminato, T., 1994. Computation of synthetic seismograms and their partial derivatives for heterogeneous media with arbitrary natural boundary conditions using the direct solution method. Geophys. J. Int. 116, 421–446.

Gudkova, T.V., P. Lognonne, and J. Gagnepain-Beyneix, 2011. Large impacts detected by the Apollo seismometers: impactor mass and source cutoff frequency estimations. Icarus 211, 1049–1065.

Harder, H., 1998. Phase transitions and the three-dimensional planform of thermal convection in the Martian mantle. J. Geophys. Res. 103, 16775–16797.

Harder, H., Schubert, G., 2001. Sulfur in Mercury's core? Icarus 151, 118–122.

Hauck, S.A., II, Dombard, A.J., Phillips, R.J., Solomon, S.C., 2004. Internal and tectonic evolution of Mercury. Earth Planet. Sci. Lett. 222, 713–728.

Holsapple, K.A., 1993. The scaling of impact processes in planetary sciences. Annu. Rev. Earth Planet. Sci. 21, 333–373.

Hughes, H.G., App, F.N., McGetchin, T.R., 1977. Global seismic effects of basin-forming impacts. Phys. Earth. Planet. Inter. 15, 251–263.

Jaeger, J.C., Cook, N.G.W., 1979. Fundamentals of Rock Mechanics, 3rd ed. Chapman and Hall, New York, 593 pp.

Kawai, K., Takeuchi, N., Geller, R.J., 2006. Complete synthetic seismograms up to 2 Hz for transversely isotropic spherically symmetric media. Geophys. J. Int. 164, 411–424.

Kanamori, H., 2006. The radiated energy of the 2004 Sumatra-Andaman earthquake. In: Abercrombie, R., McGarr, A., Di Toro, G., Kanamori, H., (Eds.), Earthquakes: Radiated Energy and the Physics of Faulting. Geophysical Monograph Series, vol. 170, American Geophysical Union, Washington, D.C., pp. 59–68.

Komatitsch, D., Barnes, C., Tromp, J., 2000. Simulation of anisotropic wave propagation based upon a spectral element method, Geophysics 65, 1251–1260.

Latham, G., Ewing, M., Dorman, J., Press, F., Toksöz, N., Sutton, G., Meissner, R., Duennebier, F., Nakamura, Y., Kovach, R., Yates, M., 1970a. Seismic data from man-made impacts on the Moon. Science 170, 620–626.

Latham, G.V., McDonald, W.G., Moore, H.J., 1970b. Missile impacts as sources of seismic energy on the Moon. Science 168, 242–245.

Lewis, J.S., 1972. Metal/silicate fractionation in the solar nebula. Earth Planet. Sci. Lett. 15, 266–290.

Margot, J.L., Peale, S.J., Jurgens, R.F., Slade, M.A., Holin, I.V., 2007. Large longitude libration of Mercury reveals a molten core. Science 316, 710–714.

McGarr, A., Latham, G.V., Gault, D.E., 1969. Meteoroid impacts as sources of seismicity on the Moon. J. Geophys. Res. 74, 5981–5994.

Melosh, H.J., 1989. Impact Cratering: A Geologic Process. Oxford University Press, New York, 253 pp.

Melosh, H.J., McKinnon, W.B., 1988. The tectonics of Mercury. In: Vilas, F., Chapman, C.R., Matthews, M.S. (Eds.), Mercury. University of Arizona Press, Tucson, Ariz., pp. 374–400.

Murchie, S.L., Watters, T.R., Robinson, M.S., Head, J.W., Strom, R.G., Chapman, C.R., Solomon, S.C., McClintock, W.E., Prockter, L.M., Domingue, D.L., Blewett, D.T., 2008. Geology of the Caloris basin, Mercury: a view from MESSENGER. Science 321, 73–76.

Murray, B.C., Belton, M.J.S., Danielson, G.E., Davies, M.E., Gault, D.E., Hapke, B., O'Leary, B., Strom, R.G., Suomi, V., Trask, N., 1974. Mercury's surface: preliminary description and interpretation from Mariner 10 pictures. Science 185, 169–179.

Purucker, M.E., Sabaka, T.J., Solomon, S.C., Anderson, B.J., Korth, H., Zuber, M.T., Neumann, G.A., 2009. Mercury's internal magnetic field: constraints on large- and small-scale fields of crustal origin. Earth Planet. Sci. Lett. 285, 340–346.

Sanloup, C., Guyot, F., Gillet, P., Fei, Y., 2002. Physical properties of liquid Fe alloys at high pressure and their bearings on the nature of metallic planetary cores. J. Geophys. Res. 107, 2272, doi:10.1029/2001JB000808.

Schubert, G., Ross, M.N., Stevenson, D.J., Spohn, T., 1988. Mercury's thermal history and the generation of its magnetic field. In: Vilas, F., Chapman, C.R., Matthews, M.S. (Eds.), Mercury. University of Arizona Press, Tucson, Ariz., pp. 429–460.

Schultz, P.H., 1988. Cratering on Mercury: a relook. In: Vilas, F., Chapman, C.R., Matthews, M.H. (Eds.), Mercury. University of Arizona Press, Tucson, Ariz., pp. 274–335.

Schultz, P.H., Gault, D. E., 1975. Seismic effects from major basin formations of the Moon and Mercury. Moon 12, 159–177.

Siegfried, R.W., II, Solomon, S.C., 1974. Mercury: internal structure and thermal evolution. Icarus 23, 192–205.

Solomon, S.C., McNutt, R.L., Jr., Gold, R.E., Acuña, M.H., Baker, D.N., Boynton, W.V., Chapman, C.R., Cheng, A.F., Gloeckler, G., Head, J.W., III, J., Krimigis, S.M., McClintock, W.E., Murchie, S.L., Peale, S.J., Phillips, R.J., Robinson, M.S., Slavin, J.A., Smith, D.E., Strom, R.G., Trombka, J.I., Zuber, M.T., 2001. The MESSENGER mission to Mercury: scientific objectives and implementation. Planet. Space Sci. 49, 1445–1465.

Solomon, S.C., McNutt, R.L., Jr., Gold, R.E., Domingue, D.L., 2007. MESSENGER mission overview. Space Sci. Rev. 131, 2–29.

Stein, S., Wysession, M., 2003. An Introduction to Seismology, Earthquakes, and Earth Structure. Blackwell Publishing, Oxford, 498 pp.

Stixrude, L., Lithgow-Bertelloni, C., 2005. Thermodynamics of mantle minerals – I: Physical properties. Geophys. J. Int. 162, 610–632.

Uno, H., Johnson, C.L., Anderson, B.J., Korth, H., Solomon, S.C., 2009. Modeling Mercury's internal magnetic field using smooth inversions. *Earth Planet. Sci. Lett.* 285, 328–339.

Takeuchi, H., Saito, M., 1972. Seismic surface waves. In: Bolt, B.A., Alder, B., Fernbach, S. Rotenberg, M. (Eds.), Methods in Computational Physics, vol. 11. Academic Press, New York, 217–295.

Watts, A.W., Greeley, R., Melosh, H.J., 1991. The formation of terrains antipodal to major impacts. Icarus 93, 159–168.

Williams, D.A., Greeley, R., 1994. Assessment of antipodal-impact terrains on Mars. Icarus 110, 196–202.

Zuber, M. T., Aharonson, O., Aurnou, J.M., Cheng, A.F., Hauck, S.A., II, Heimpel, M.H., Neumann, G.A., Peale, S.J., Phillips, R.J., Smith, D.E., Solomon, S.C., Stanley, S., 2007. The geophysics of Mercury: current knowledge and future opportunities. Space Sci. Rev.131, 105–132.